Nature Communications

https://doi.org/10.1038/s41467-026-70635-5

Article in Press

Rapid subsurface warming in the subpolar North Atlantic from freshening

Received: 10 June 2025

Accepted: 2 March 2026

Cite this article as: Menviel, L.C., Pontes, G., Lapeze, M. *et al.* Rapid subsurface warming in the subpolar North Atlantic from freshening. *Nat Commun* (2026). https://doi.org/10.1038/s41467-026-70635-5

Laurie C. Menviel, Gabriel Pontes, Mathieu Lapeze & Himadri Saini

Rapid subsurface warming in the subpolar North Atlantic from freshening

Laurie C. Menviel[1,2,*], Gabriel Pontes[1,2,3], Mathieu Lapeze[1,4], and Himadri Saini[1,5]

[1]Climate Change Research Centre, University of New South Wales, Sydney, Australia
[2]The Australian Centre for Excellence in Antarctic Science, University of New South Wales, Sydney, Australia
[3]School of Earth and Environment, University of Leeds, Leeds, LS2 9JT, West Yorkshire, UK
[4]Department of Energy and Process Engineering, Norwegian University of Science and Technology, Trondheim, Norway
[5]School of Geography, Earth and Atmospheric Sciences, The University of Melbourne, Victoria 3010 Australia
[*]Corresponding author, l.menviel@unsw.edu.au

ABSTRACT

Over recent decades, the Arctic has warmed four times faster than the global average, associated with a decline in sea ice and accelerating Greenland Ice Sheet mass loss, which has contributed to episodic freshening of the subpolar North Atlantic. Here, we show that a 0.05 Sv North Atlantic meltwater flux induces ∼1°C subsurface warming within a decade in Baffin Bay, Hudson Strait, and along Greenland's southern and western coasts. This warming arises from enhanced stratification, weakened deep convection in the subpolar gyre, and a weaker Labrador Current. Freshening also alters horizontal density gradients, strengthening cyclonic circulation in the Nordic Seas and causing transient regional warming. The temperature response significantly depends on the location of deep-ocean convection, highlighting the need for simulations with accurate deep-ocean convection. This warming may create a positive feedback, accelerating Greenland and Arctic glacier melt with implications for ice-sheet stability and the strength of the Atlantic Meridional Overturning Circulation.

1 Introduction

Since 1979, Arctic sea ice has declined at an unprecedented rate, with summer sea-ice extent decreasing by 12% per decade (1; 2). Arctic sea-ice thickness also decreased, thus leading to a ∼43% decline in Arctic summer sea-ice volume since 1994 (3). Because sea-ice reflects a large fraction of incoming solar radiation, its loss amplifies the Arctic warming through the ice-albedo feedback, contributing to Arctic temperatures rising about four times faster than the global average (4). As a result, Greenland ice-sheet loss has accelerated from about 42 Gt/yr in 1992-2001 to 235 Gt/yr in 2012-2020 (5).

These changes likely affected the freshwater budget of the Arctic and subpolar North Atlantic (6). Subpolar North Atlantic freshening has been documented in the 1960s - early 1970s, and since the mid-1990s, both at the surface and at depth (7; 8; 9; 10; 11), while Arctic freshening has also been observed over recent decades (9; 12). Several episodes of extreme freshening have been recorded in the subpolar North Atlantic. The late 1960s to early 1970 Great Salinity Anomaly, driven by enhanced sea ice export from the Arctic (13), was equivalent to a freshwater discharge of up to 0.065 Sv (1 Sv = $10^6 m^3/s$) into the subpolar North Atlantic (8). Between 2012 and 2016, another pronounced freshening event occurred, and was attributed to anomalous winter wind patterns (14) and/or an increased outflow of relatively fresh, cold surface waters from the Labrador Sea (15). In addition, Greenland ice-sheet and Arctic glaciers melt since the 1990s led to a mean increase in runoff and ice discharge in the subpolar North Atlantic of about 0.013 Sv (16), reaching up to ∼0.04 Sv in 2012 (17).

This subpolar North Atlantic freshening is not captured by simulations from the Coupled Model Intercomparison Project (CMIP) phase 6 (CMIP6) (10), potentially because CMIP6 historical simulations underestimate the Arctic sea-ice decline (18) and/or do not include past and future changes in Greenland runoff. However, through their impact on ocean stratification,

and the strength and location of deep-water formation, Arctic and subpolar North Atlantic freshening could affect subpolar North Atlantic climate as well as the Atlantic Meridional Overturning Circulation (AMOC), which plays a crucial role in shaping global climate. The deep limb of the AMOC originates from the formation of North Atlantic Deep Water in the Nordic, Irminger and Labrador Seas (19) as well as Icelandic basin (20), and flows southward at potential density levels of about 1035.7 to 1036.7 kg/m^3 (referenced to 2000 dbar, Fig. S1a,c), equivalent to a depth range of ∼500 to 2500 m. As such, the strength of the AMOC is tied to deep-water formation rates and therefore upper-layer density and vertical density gradients. Observational evidence indicates that the AMOC is at its weakest over the last millennium (21), with some studies suggesting a ∼15% weakening since the mid-20th century (22; 23; 24; 25), potentially linked to freshening (26). However, long-term AMOC trends are inferred using fingerprints or proxies and are thus associated with high uncertainty (e.g. 27), and the relatively short direct AMOC observational record (28; 29) means that recent changes could also simply reflect large AMOC decadal-scale variability (30; 31).

Subpolar North Atlantic freshening significantly impacted the AMOC in the past. In particular during Heinrich events of the last glacial period and deglaciations, when iceberg discharges in the North Atlantic, which are estimated to have contributed a flux of 0.003 to 0.13 Sv (32), weakened the AMOC substantially (33; 34), but also during the 8.2 ka event in the early Holocene, when the collapse of the Hudson Bay ice saddle likely added as much as 0.6 Sv of meltwater into the Labrador Sea over the course of 100 years, further disrupting the AMOC (35).

While the century-scale climatic impact of large (>0.1 Sv) subpolar North Atlantic freshening and associated AMOC weakening have been extensively investigated (36; 37; 38), the decadal-scale effect of small to moderate freshening on both surface and subsurface temperatures remains poorly constrained. Given that the Greenland ice-sheet retreat is projected to continue over the coming century, with a possible exponential increase in melting rate up to 0.084 Sv between 2080 and 2099 in high-emissions scenario SSP5-8.5 (39), a better understanding of the impact of decadal-scale subpolar North Atlantic freshening is needed. Here, we assess the multi-decadal impact of subpolar North Atlantic freshening on the subpolar North Atlantic and Nordic Seas, using historical and future simulations forced with a bespoke meltwater input, as well as idealized simulations performed with the Australian Earth system model ACCESS-ESM1.5 (40) and the eddy-permitting ocean/sea-ice ACCESS-OM2-025 model (41).

2 Results

Impact of subpolar North Atlantic freshening over the coming century

To account for the underestimated subpolar North Atlantic freshening during the historical period, as well as the current and projected accelerated melting of the Greenland ice-sheet and Arctic glaciers (5; 16; 39; 42; 43), we perform an ensemble of historical and SSP5-8.5 simulations following the CMIP6 protocol but with meltwater input into the subpolar North Atlantic (Hist-SSP585-FW, Methods, Table S1, mask 1 Fig. S2). The meltwater input is idealized and higher than current and projected estimates (17; 43), but it was scaled on the historical period to simulate a decadal-scale AMOC variability and multi-decadal AMOC trend in agreement with direct AMOC measurements and AMOC indices (26). Over the 21st century, the freshwater forcing follows a simple linear relationship from historical to projected Greenland surface air temperature changes (26). The meltwater input amounts to 0.05 Sv in 1960-1989 and 2000-2004, 0.075 Sv in 2005-2019, and increases with a decadal timestep to reach 0.275 Sv in 2090 (Fig. 1a). Here we analyze the climatic differences between the ensemble of historical and SSP5-8.5 simulations with and without subpolar meltwater input (Hist-SSP585-FW compared to Hist-SSP585), focusing on years 1980-1989, and 2030-2039, when the system responds to moderate meltwater fluxes, and the end of the century (2090-2099), which provides an estimate of the impact of large meltwater fluxes.

In Hist-SSP585, rising greenhouse gas concentrations (Methods) (44) lead to a pronounced weakening of deep-water formation in the Nordic Seas and, to a lesser extent, in the subpolar gyre (Fig. S3d-f). This results in a gradual AMOC decline from 16.3 Sv in 1980-1989 to 13.5 Sv in 2030-2039 and 10.5 Sv in 2090-2099 (Fig. 1b, black), consistent with observationally constrained CMIP6 AMOC projections (45). The inclusion of meltwater in the subpolar North Atlantic further weakens

deep-water formation in the subpolar gyre (Fig. 2e,j,o), with a collapse of deep-ocean convection in the North Atlantic subpolar gyre in 2030-2039 and 2090-2099 in Hist-SSP585-FW (Fig. 2 j,o). This accelerates the AMOC decline, with the AMOC reaching 10.6 Sv in 2030-2039 and 8.3 Sv in 2090-2099 in Hist-SSP585-FW (Fig. 1b, blue). The AMOC is thus 35% and 49% weaker than its pre-industrial state in Hist-SSP585-FW in 2030-2039 and 2090-2099, respectively, compared to reductions of 17% and 36% in Hist-SSP585.

The weaker deep-ocean convection in the subpolar gyre along with the reduced surface density in the subpolar North Atlantic in Hist-SSP585-FW compared to Hist-SSP585 significantly affects the circulation and temperature in the subpolar North Atlantic and Nordic Seas. A surface cooling is simulated in the North Atlantic, particularly on the eastern edge of the subpolar gyre (Figs. 1d and 2a,f,k). This cooling reaches -0.9±=0.4°C and -1.9±0.9°C on the eastern edge of the subpolar gyre in 1980-1989 and 2030-2039, respectively, and extends across the North Atlantic at the end of the century (Fig. 2a,f,k).

On the other hand, SSTs in the center of the Nordic Seas and Baffin Bay are higher in Hist-SSP585-FW than Hist-SSP585 from the 2030s. In 2030-2039, the surface warming amounts to 0.2 °C in Baffin Bay (1σ=0.1°C, decadal mean across ensemble members) and 0.8°C in the Nordic Seas (1σ=0.8°C) (Figs. 1e,g and 2f). At the end of the century, the warming in Hist-SSP585-FW compared to Hist-SSP585 is more pronounced and completely covers the Nordic Seas as well as the Barents Sea, while it is reduced in Baffin Bay (Figs. 1e,g and 2k). These SST anomalies are associated with a loss of sea-ice on the western side of the Nordic Seas and to a lesser extent on the western side of the Labrador Sea in 2030-2039 (Fig. S4d). As a result, annual mean surface air temperature is also higher by ∼2°C in the central Nordic Seas and 0.5°C in the Labrador Sea in 2030-2039, with this warming extending over the entire Nordic and Barents Seas in 2090-2099 (Fig. S4c,e).

In the Nordic Seas, the positive temperature anomalies are maximum in the top 100 m and decrease with depth, but remain positive until ∼600 m depth (Fig. 1g). Between 100 and 400 m depth, a 0.4°C temperature increase is simulated in the central Nordic Seas at years 2030-2039 (Fig. 2g). From ∼2070, the subsurface temperature in the Nordic Seas rises sharply, reaching +1°C in 2090-2099, with the warming extending across the entire Nordic and Barents Seas (Figs. 1g and 2l).

In the North Atlantic, Labrador Sea, Hudson Strait and Baffin Bay, a subsurface warming is simulated even with a 0.05 Sv freshwater input and within about 10 years of the meltwater addition. During 1980-1989, a significant 0.5 to 1.5°C warming is simulated in these regions between 100 and 400 m depth (Fig. 2b). Maximum positive anomalies are simulated between 100 and 200 m depth, where they reach +2°C in 2030-2039 (Fig. 1d,e,f). The simulated subsurface warming in the North Atlantic subpolar gyre decreases from the 2060s, while it increases in the eastern side of the North Atlantic (Figs. 1d and 2g,l), as deep-ocean convection on the western side of the subpolar gyre also weakens in Hist-SSP585 (Fig. S3f).

Processes leading to the ocean temperature changes

A heat budget analysis reveals that the simulated temperature changes in the top 50 m are driven by variations in ocean heat transport convergence, with air-sea heat fluxes simply responding to the changes in ocean heat convergence (Fig. 3). As meltwater is added to the subpolar North Atlantic, it is entrained by the subpolar gyre, resulting in a decrease in surface density and enhanced stratification, especially along the edges of the subpolar gyre. In 1980-1989, the decrease in surface density and associated increase in stratification are centered in the western subpolar gyre (Fig. 2c,d). The sustained meltwater input leads to the advection of freshwater into the eastern part of the subpolar gyre and the Iceland basin in 2030-2039, with a further intensification towards 2090-2099 (Fig. 2h,m). This modified zonal density gradient alters the structure of the subpolar gyre, reducing its intensity (Fig. S5, top).

The reduced density in the subpolar North Atlantic generates downwelling Kelvin waves, that move southward along the North American coast (26). The downwelling Kelvin waves, along with weaker deep-ocean convection, lead to a weakening of the Gulf Stream (26) (Fig. S5d-f), and thus of the northward oceanic heat transport. As a result, in the North Atlantic subpolar gyre at years 2090-2099, the ocean heat transport convergence weakens by an average of 47 W/m^2 in the top 50 m (Fig. 3f), leading to reduced heat loss to the atmosphere by 33 W/m^2 (Fig. 3e) and 14 W/m^2 lower ocean heat content compared to experiments SSP585 (Fig. 2k).

On the other hand, increased stratification (Fig. 2d,i,n) and reduced convective mixing (Fig. 2e,j,o) in the North Atlantic

lead to a subsurface warming through reduced injection of cold surface waters to depth (Figs. 2b,g,l and 4). This occurs despite reduced meridional temperature advection associated with the weaker Gulf Stream (Figs. S5d-f and S6c). Enhanced stratification also explains the simulated subsurface warming in the Labrador Sea and Baffin Bay by limiting mixing between cold surface waters and relatively warmer subsurface waters (Figs. 4 and S6e).

While the heat transport convergence decreases in most of the North Atlantic subpolar gyre, it increases around the Hudson Strait, Labrador Shelf and in the Nordic Seas (Fig. 3b,d,f). The positive heat transport convergence anomalies around the Hudson Strait, and along the Labrador Shelf result from the weaker southward Baffin Island and Labrador Currents, linked to the weakening of the subpolar gyre (Figs. 4 and S5d,e).

In the Nordic Seas, heat transport convergence increases by about 34 W/m^2 during 2090-2099 (Fig. 3f), leading to enhanced heat loss to the atmosphere by 24 W/m^2 (Fig. 3e) and an increase in ocean heat content of 10 W/m^2 (Figs. 2k, S5a). From the 2070s, this higher heat transport convergence is driven by a strengthening of the Atlantic inflow by up to 50% (Figs. S5f and S6a, grey). This intensified Atlantic inflow explains the widespread surface and subsurface warming that develops in the Nordic Seas and Barents Sea from the 2070s (Figs. 2k,l and 5c, blue circles). The strengthening of the Atlantic inflow results from an increase in the density gradient between the Nordic Seas and the North Atlantic (Fig. 5, blue circles). While there are changes in surface winds, a decomposition of the current changes into Ekman-driven and geostrophic currents confirms the dominance of geostrophic currents (46) (not shown).

A 1.5°C surface warming is however already simulated in the central Nordic Seas at years 2030-2039 (Fig. 2f), without a substantial increase in the Atlantic inflow (Fig. S5e). The meridional and zonal density anomalies resulting from the freshwater input lead to a strengthening of the cyclonic circulation in the Nordic Seas (Fig. 2h,m, Fig. 5, blue circles and Fig. S5b). As the surface density is highest on the eastern and northern side of the Nordic Seas, this stronger circulation leads to a density increase in the central Nordic Seas through advection of relatively salty waters to the centre of the Nordic Seas (Fig. 2h,m). This deepens the mixed layer in the region and enhances mixing, thus leading to surface warming (Figs. 2f,j,k,o and S6a, magenta).

Responses of the subpolar North Atlantic and Nordic Seas to idealized meltwater fluxes

To assess the robustness of the results described above, their sensitivity to meltwater flux and location, and their model-dependence, we perform an ensemble of idealized simulations with the ACCESS-ESM1.5 and with the eddy-permitting ocean-sea-ice ACCESS-OM2-025 model (Table S1, Methods). An ACCESS-ESM1.5 experiment performed under constant pre-industrial conditions and with North Atlantic meltwater input of 0.05 Sv (FW005-ESM, Table S1) provides similar results to those found in Hist-SSP585-FW at the end of the 20th century (Fig. 6). The freshwater input weakens deep-water formation in the North Atlantic subpolar gyre and northern Nordic Seas, leading to a 2 Sv AMOC weakening within two decades (Figs. 6e, S1b and S7 magenta, significant at the 99% level using a Kolmogorov-Smirnov test). These changes lead to a surface cooling in the North Atlantic (Fig. 6a), particularly in the subpolar gyre, and a strong (∼1.5°C) subsurface warming in Baffin Bay, the Labrador Sea and the northwest Atlantic (Fig. 6b). This subsurface warming is due to increased stratification resulting from the surface density decrease (Fig. 6c,d).

As highlighted in the Hist-SSP585-FW simulations, as the meltwater increases, so does the climatic response. A large (0.4 Sv) meltwater input in the North Atlantic leads to a collapse of deep-ocean convection in the subpolar gyre, a 4°C surface cooling in the eastern side of the subpolar gyre, but a 2°C surface warming in the central Nordic Seas due to stronger Atlantic inflow (Figs. 5 and S8a). The addition of meltwater to the North Atlantic initially reduces the density in this region, before affecting the Nordic Seas. This results in an enhanced density contrast between the Nordic Seas and the North Atlantic, which in turn strengthens the Atlantic inflow (Fig. 5b,c). Consequently, a large (≥2°C) subsurface warming is simulated in the Nordic Seas, extending into the Barents Sea (Fig. S8b). Due to the greater stratification (≥2 kg/m^3), and reduced mixing, a large (+3.5°C) subsurface warming is simulated in Baffin Bay, the Labrador Sea and most of the North Atlantic, with a pattern similar to the one obtained in Hist-SSP585-FW compared to Hist-SSP585 at years 2090-2099 (Fig. 2l and S8). The sensitivity experiments performed with the ACCESS-ESM1.5 thus confirm the results obtained in the historical and future simulations

(Hist-SSP585-FW).

Finally, to evaluate the model dependence of the results, we analyse the impact of a moderate (0.075 Sv) meltwater input in the subpolar North Atlantic in the eddy-permitting, ACCESS-OM2-025 (FW0075-OM, Fig. 7, Table S1). The meltwater input weakens deep-water formation in the subpolar gyre (Fig. 7e) and the AMOC by 30% (Figs. S1d and S7 cyan), which leads to a strong ($\geq$2°C) surface cooling in the subpolar gyre (Fig. 7a). Due to the modified zonal density gradient in the North Atlantic, the North Atlantic current weakens and shifts towards the east, which leads to a surface warming in the Icelandic basin. Similar to the ACCESS-ESM1.5, the cyclonic gyre in the Nordic Seas strengthens and so does the Atlantic inflow (Fig. 5, triangles), leading to both a surface and subsurface warming in the central Nordic Seas (Fig. 7a,b).

On the other hand, the subsurface warming is limited to the narrow Greenland coastal and Labrador currents, and the North Atlantic subsurface warming is restricted to the Icelandic basin and eastern North Atlantic. While the subsurface temperature response differs substantially in the two models, in all experiments, the North Atlantic subsurface warming arises in areas that display a significant surface density decrease, and thus increased stratification (Figs. 6c,d and 7c,d). The subsurface warming in the Hudson strait and the Labrador shelf results from the incursion onto the shelf of warm subsurface waters from the Labrador Sea, due to a flattening of the isopycnals and weaker Baffin Island and Labrador currents (Fig. 4).

An additional simulation performed with the ACCESS-OM2-025 (FW0075GC-OM, Table S1) shows that meltwater addition close to the coast of Greenland (mask 3 in Fig. S2), instead of over a uniform area around Greenland (mask 1 in Fig. S2), broadly leads to a similar pattern of surface and subsurface temperature anomalies (Figs. 7 and S9). However, enhanced meltwater addition on the Greenland coast does not lead to a subsurface warming around the southern tip of Greenland (Fig. S9b) as the cooling can penetrate a few hundred meters over the shelf, which is very shallow at this location. In addition, more efficient export of meltwater around the gyre in that experiment strengthens stratification in the Hudson Strait and on the Labrador shelf leading to a stronger subsurface warming in these regions in FW0075GC-OM than FW0075-OM (Figs. 7 and S9).

Nevertheless, the location of meltwater addition has a relatively small influence on the temperature response compared to the differences between experiments performed with the ACCESS-ESM1.5 and ACCESS-OM2-025. Although some of these differences could result from the lack of atmosphere coupling or higher spatial resolution in the ACCESS-OM2-025 (47), the location of deep convection seems to be the dominant factor controlling the temperature response to subpolar North Atlantic freshwater input.

As can be seen from the March mixed layer depth (Fig. S3), while convection is very strong in the Labrador Sea in the ACCESS-OM2-025 control run, it is weak in the ACCESS-ESM1.5 pre-industrial and historical experiments. A small meltwater input thus rapidly stratifies the Labrador Sea and Baffin Bay in the ACCESS-ESM1.5, potentially leading to a collapse of deep-water formation in the subpolar gyre (Fig. 2j,o), whereas the Labrador Sea convection site remains strong in the ACCESS-OM2-025 (Fig. 7e), thus affecting the freshwater transport in the subpolar gyre and bringing cold water to depth. As the meltwater input increases in the ACCESS-OM2-025, the convection in the Labrador Sea weakens and the extent and magnitude of the subsurface warming in the Labrador Sea and North Atlantic increase (Fig. S8g,j), becoming similar to the ACCESS-ESM1.5 response (Fig. S8b). Similarly, the lack of surface warming in the Nordic Seas for meltwater inputs of about 0.05 Sv in the ACCESS-ESM1.5 experiments (Hist-SSP585-FW at years 1980-1989 and FW005-ESM), compared to the pronounced warming simulated in the ACCESS-OM2-025 experiments (FW0075-OM and FW0075GC-OM) may be attributed to the relatively strong deep-ocean convection in the Nordic Seas in the ACCESS-ESM1.5 in the pre-industrial and historical experiments (Fig. S3b,d).

3 Discussion

While there is evidence of accelerated melting of the Greenland ice-sheet and Arctic glaciers over the last decades (5; 16; 42), CMIP6 protocols for historical and future projections do not include meltwater and ice discharge to the subpolar North Atlantic. An ensemble of historical and SSP5-8.5 simulations following the CMIP6 protocol but with meltwater input to the subpolar

North Atlantic (26) (Hist-SSP585-FW, Methods) displays a faster and stronger AMOC weakening than standard CMIP6 simulations (Hist-SSP585), but still within the range of AMOC weakening simulated in CMIP6 SSP5-8.5 simulations over the 21st century (48). These simulations also display a collapse of deep-water formation in the North Atlantic subpolar gyre for meltwater pulses greater than 0.1 Sv.

Although the North Atlantic meltwater input increases stratification in the subpolar North Atlantic thus reducing the surface North Atlantic warming over the coming century, it could intensify the surface warming in the Nordic Seas, and the subsurface warming to the west and south of Greenland, in Baffin Bay, the Hudson Strait, and the Labrador Sea. Even though the meltwater input in these simulations is overestimated, a substantial climatic response emerges for moderate (0.05 Sv) meltwater inputs. For context, the late 1960s-early 1970 Great Salinity Anomaly was associated with a freshwater anomaly of 0.065 Sv (8), and combined Greenland meltwater and ice discharge are projected to reach 0.084 Sv during the 21st century (39; 43). Consistent with these findings, results from idealized meltwater experiments performed under constant pre-industrial conditions show that a subsurface warming of up to 2°C can develop around the western, southern and southeastern coasts of Greenland in less than 20 years with a meltwater input of 0.05 Sv.

Standard CMIP6 SSP5-8.5 experiments project a subsurface warming in the North Atlantic over the coming century, primarily associated with increased ocean heat uptake under higher radiative forcing (Fig. S10a,b,d,e). Although enhanced stratification may also contribute to this subsurface warming (Fig. S10c,f), a formal attribution of these processes has not been performed. In the Hist-SSP585-FW experiments, freshwater-induced stratification amplifies the subsurface warming across the North Atlantic - potentially doubling its magnitude over the coming decades around Greenland, and doubling it in the eastern North Atlantic and Nordic Seas at the end of the century when radiative forcing becomes the dominant driver.

Although the surface cooling in the subpolar gyre is a consistent feature of weakened deep-ocean convection in the subpolar gyre (23; 37; 49), the subsurface and Nordic Sea temperature responses are model-dependent, and in particular dependent on the strength and location of deep-ocean convection. The subsurface warming simulated in Baffin Bay, the Labrador Sea and the North Atlantic is significantly greater in the ACCESS-ESM1.5 than in the eddy-permitting ACCESS-OM2-025 and in previous studies (50) because deep-ocean convection in the Labrador Sea is weak in ACCESS-ESM1.5 pre-industrial and historical simulations (Fig. S3b,d). As a result, even a small meltwater input in the subpolar North Atlantic effectively stratifies the Labrador Sea in the ACCESS-ESM1.5 (Fig. 6), leading to substantial and widespread subsurface warming. In contrast, due to the strong convection in the Labrador Sea in the ACCESS-OM2-025 (Fig. S3a), convection is still strong with a 0.075 Sv meltwater input (Fig. 7e). Comparison with observations (51) (Fig. S3c) indicates that Labrador Sea convection is too strong in the ACCESS-OM2-025, whereas it is too weak in the ACCESS-ESM1.5. Consequently, the simulated subsurface warming in Baffin Bay and the Labrador Sea is likely overestimated in ACCESS-ESM1.5 and underestimated in ACCESS-OM2-025. In contrast, comparison with observations suggests that deep-ocean convection may be too strong in the Nordic Seas in the ACCESS-ESM1.5, raising the possibility of enhanced Nordic Sea warming over the coming decades.

For meltwater inputs greater than 0.075 Sv, in addition to the previously mentioned subsurface warming, reduced deep water formation and changes in zonal density gradients drive a stronger cyclonic flow in the Nordic Seas ∼30 years after the initiation of the forcing. This enhanced flow induces a surface warming in the central Nordic Seas through a deepening of the mixed layer. This SST increase further leads to a sea-ice decrease and a rise in surface air temperature in that region. A similar response is simulated in future simulations of the Large Ensemble project of the Community Earth System Model (CESM-LE) (52), where an enhanced zonal density gradient strengthens the cyclonic circulation in the Nordic Seas, thereby intensifying the overturning circulation. This surface warming in the central Nordic Seas arises from an initial state with weak convection in the Nordic Seas in the ACCESS-OM2-025 and Hist-SSP585 at years 2030-2039, and in line with current observations (Fig. S3a,e). This surface warming in the Nordic Seas is not simulated in FW005-ESM because the convection is strong in the Nordic Seas in the ACCESS-ESM1.5 PI control state (Fig. S3b). In addition, when the density difference between the Nordic Seas and the North Atlantic increases, the Atlantic inflow to the Nordic Seas increases (Fig. 5), which drives a strong ($\geq$2°C) warming, both at the surface and in the subsurface of the Nordic and Barents Seas.

This study thus further highlights how the location and intensity of deep-ocean convection in the North Atlantic, Labrador Sea and Nordic Seas modulate the climatic response to surface freshening, and arguably to surface warming as well. The mixed layer biases identified in both the ACCESS-ESM1.5 and ACCESS-OM2-025 are common to many coupled climate models (e.g. CMIP5 (53)) and ocean/sea-ice models (54), underscoring the need to improve the understanding and representation of North Atlantic Deep Water formation in both present and past climates. The rapid and significant subsurface temperature response to increased stratification, and the strong dependence on the strength and location of deep-water formation has implications for both past and future climate. For example, small freshwater perturbations to a relatively stratified Labrador Sea during glacial times would have led to a subsurface warming in the Labrador Sea and Hudson Strait, ultimately triggering Laurentide ice-sheet discharges and Heinrich events - consistent with the sequence of events inferred from proxy records (55).

Although the freshwater forcing used in our Hist-SSP585-FW simulations is idealized and overestimated based on present knowledge, recent Greenland ice-sheet projections display an accelerated sea-level contribution over the coming century, the uncertainties associated with the rate of changes are still large (43; 56), and Greenland ice-sheet simulations do not incorporate climate feedbacks from ice-sheet loss. In addition, our simulations reveal a pronounced temperature response even with a meltwater flux of 0.05 Sv, indicating that the system is sensitive to freshwater perturbations of a magnitude that has occurred episodically over recent decades (17; 57) and could persist into the coming century. Both the surface and subsurface response are sensitive to the location of the meltwater input, with enhanced input in the Baffin Bay and Labrador Sea particularly affecting subsurface temperatures in that region, while freshening anomalies in the eastern Atlantic particularly impact the Nordic and Barents Seas.

Although oceanic forcing has a relatively minor impact on the dynamics of the Greenland ice-sheet compared to the Antarctic ice-sheet (58), the Greenland ice-sheet and its periphery are home to 745 marine terminating glaciers, with over 300 in the Canadian Arctic and 166 in Svalbard (59). Between 2000 and 2020, about 85% of these marine terminating glaciers retreated (59), with evidence of ocean warming driving the glaciers retreat around Svalbard (60). The simulated subsurface warming around Greenland, particularly on the western and southern sides, could thus provide a positive feedback to the Greenland melting.

Methods

We assess the impacts of a subpolar North Atlantic freshening on climate by performing an 8-member ensemble of historical and 21st century SSP5-8.5 simulations with subpolar North Atlantic meltwater input with the Australian Community Climate and Earth System Simulator-Earth System Model version 1.5 (ACCESS-ESM1.5) (40). To assess the robustness of the results, idealized North Atlantic meltwater experiments are performed from the pre-industrial control state with the ACCESS-ESM1.5 and from a modern neutral repeat year forcing with the eddy-permitting ocean/sea-ice model ACCESS-OM2-025 (41).

Models

The ACCESS-ESM1.5 includes the UK Met Office Unified Model (UM) version 7.3 (61) at N96 resolution (1.875°×1.25° and 38 vertical levels) as the atmospheric model, coupled to the land surface model, the Community Atmosphere Biosphere Land Exchange model (CABLE) version 2.4 (62). The NOAA/GFDL Modular Ocean Model (MOM) version 5 (63) (1°×1° horizontal resolution increasing to 0.4° in the Southern Ocean and 0.33° near the equator, 50 vertical levels) is the ocean model, and is coupled to the Los Alamos National Laboratory sea-ice model (LANL CICE) version 4.1 (64).

The ACCESS-OM2-025 includes MOM version 5.1 with a nominal horizontal resolution of 0.25° and 50 vertical levels. It is coupled to the Los Alamos sea ice model (CICE) version 5.1.2. The atmospheric forcing repeats the neutral year cycle from May 1990 to April 1991 (repeat year forcing), taken from 55-year Japanese Reanalysis for driving oceans (JRA55-do) (65).

Historical and future projections simulations

Historical and future SSP5-8.5 simulations are performed with the ACCESS-ESM1.5 following the CMIP6 protocols but with meltwater addition in the subpolar North Atlantic (Hist-SSP585-FW, Table S1). These are compared to standard CMIP6 historical and SSP5-8.5 simulations (Hist-SSP585) (44; 66). In Hist-SSP585-FW simulations, meltwater is added in the subpolar North Atlantic (59°N-72°N and 65°W-22°W, mask 1, Fig. S2) starting year 1960 (26). The meltwater flux imposed in

the historical simulations and future projections is shown in Fig. 1a. To a first order, this meltwater input is scaled on Greenland warming. The meltwater addition amounts to 0.05 Sv (1 Sv is $10^6 m^3/s$) in the 20th century - apart from 1990 to 1999, when no meltwater is added to reflect the concurrent Greenland cooling - and is increased with a decadal timestep reaching 0.075 Sv in 2015, 0.15 Sv in 2040 and 0.275 Sv in 2090. This meltwater input was designed to obtain a better representation of direct AMOC measurements and AMOC indices over the last decades, and was then scaled linearly over the 21st century (26). However, this meltwater input is higher than observational and projected estimates (8; 16; 43).

Idealized North Atlantic meltwater experiments

Idealized North Atlantic meltwater experiments are performed with the ACCESS-ESM1.5 (Table S1). They are initialized from the pre-industrial control run (*piControl*) (67), which is forced with orbital parameters corresponding to 1850 CE and an atmospheric CO_2 concentration of 284.3 ppm (68). For the ensemble of FW005-ESM, four experiments are performed with the addition of 0.05 Sv of meltwater in the same region as SSP585-FW (59°N-72°N and 65°W-22°W, mask 1, Fig. S2). For experiment FW04-ESM, 0.4 Sv of freshwater is added in in mask 1 region.

Three experiments are also performed with the ACCESS-OM2-025 (Table S1) by adding i) 0.4 Sv broadly in the North Atlantic (FW04-OM, 50°N-70°N and 70°W-0°E, mask 2, Fig. S2), ii) 0.075 Sv in mask 1 region (FW0075-OM), and iii) 0.075 Sv in mask 3 region (FW0075GC-OM). In mask 3, most of the meltwater is added close to the Greenland coast to simulate liquid runoff, while a minor portion is added over a broader region to represent ice discharge. Figure S2 displays the anomalous runoff rate ($kg/m^2/s$) that has to be divided by the water density and multiplied by the area over which the meltwater is added to obtain Sv.

The AMOC is defined as the maximum meridional overturning streamfunction in density space at 26.5°N and for potential densities between 1035 and 1037 kg/m^3 (69).

Uncertainty ranges are defined as 1 standard deviation (σ).

Oceanic heat budget

The changes in North Atlantic heat content in the top 50m can be decomposed into changes in ocean to atmosphere heat fluxes and ocean heat convergence. Net ocean to atmosphere heat fluxes are a direct output of the model. Therefore, changes in ocean heat convergence are simply calculated as the difference between changes in oceanic heat content and changes in net ocean to atmosphere heat fluxes.

Data availability The data underpinning this work is available on the public UNSWorks repository: https://doi.org/10.26190/unsworks/3183

References

1. Stroeve, J. & Notz, D. Changing state of arctic sea ice across all seasons. *Environ. Res. Lett.* **13**, 103001, 10.1088/1748-9326/aade56 (2018).

2. Meier, W. N. & Stroeve, J. An updated assessment of the changing arctic sea ice cover. *Oceanogr.* **35**, pp. 10–19 (2022).

3. Bocquet, M., Fleury, S., Rémy, F. & Piras, F. Arctic and antarctic sea ice thickness and volume changes from observations between 1994 and 2023. *J. Geophys. Res. Ocean.* **129**, e2023JC020848, https://doi.org/10.1029/2023JC020848 (2024). E2023JC020848 2023JC020848, https://agupubs.onlinelibrary.wiley.com/doi/pdf/10.1029/2023JC020848.

4. Rantanen, M. *et al.* The Arctic has warmed nearly four times faster than the globe since 1979. *Commun Earth Environ* **168**, 10.1038/s43247–022–00498–3 (2022).

5. Otosaka, I. N. *et al.* Mass balance of the Greenland and Antarctic ice sheets from 1992 to 2020. *Earth Syst. Sci. Data* **15**, 1597–1616, 10.5194/essd-15-1597-2023 (2023).

6. Jahn, A. & Laiho, R. Forced changes in the arctic freshwater budget emerge in the early 21st century. *Geophys. Res. Lett.* **47**, e2020GL088854, https://doi.org/10.1029/2020GL088854 (2020). E2020GL088854 10.1029/2020GL088854, https://agupubs.onlinelibrary.wiley.com/doi/pdf/10.1029/2020GL088854.

7. Dickson, B. *et al.* Rapid freshening of the deep North Atlantic Ocean over the past four decades. *Nat.* **416**, 832–837, 10.1038/416832a (2002).

8. Curry, R. & Mauritzen, C. Dilution of the Northern North Atlantic Ocean in recent decades. *Sci.* **308**, doi:10.1126/science1109477 (2005).

9. Rabe, B. *et al.* Arctic ocean basin liquid freshwater storage trend 1992–2012. *Geophys. Res. Lett.* **41**, 961–968, https://doi.org/10.1002/2013GL058121 (2014). https://agupubs.onlinelibrary.wiley.com/doi/pdf/10.1002/2013GL058121.

10. Molodtsov, S. *et al.* North Atlantic temperature and salinity changes are driven by external forcing, underestimated by CMIP6 models. *npj Clim Atmos Sci* **8**, 332, 10.1038/s41612-025-01210-w (2025).

11. Chomiak, L. N., Volkov, D. L., Johns, W. E., V, J. A. H. & Smith, R. H. Deep ocean cooling and freshening from Subpolar North Atlantic reaches Subtropics at 26.5°N. *Commun Earth Environ* **6**, 235, 10.1038/s43247-025-02170-y (2025).

12. Proshutinsky, A. *et al.* Analysis of the Beaufort Gyre Freshwater Content in 2003–2018. *J. Geophys. Res. Ocean.* **124**, 9658–9689, https://doi.org/10.1029/2019JC015281 (2019).

13. Häkkinen, S. An arctic source for the great salinity anomaly: A simulation of the arctic ice-ocean system for 1955–1975. *J. Geophys. Res. Ocean.* **98**, 16397–16410, https://doi.org/10.1029/93JC01504 (1993). https://agupubs.onlinelibrary.wiley.com/doi/pdf/10.1029/93JC01504.

14. Holliday, N., Bersch, M. & Berx, B. e. a. Ocean circulation causes the largest freshening event for 120 years in eastern subpolar North Atlantic. *Nat. Commun.* **11**, 10.1038/s41467-020-14474-y (2020).

15. Fox, A. D. *et al.* Exceptional freshening and cooling in the eastern subpolar north atlantic caused by reduced labrador sea surface heat loss. *Ocean. Sci.* **18**, 1507–1533, 10.5194/os-18-1507-2022 (2022).

16. Bamber, J. L. *et al.* Land Ice Freshwater Budget of the Arctic and North Atlantic Oceans: 1. Data, Methods, and Results. *J. Geophys. Res. Ocean.* **123**, 1827–1837, https://doi.org/10.1002/2017JC013605 (2018). https://agupubs.onlinelibrary.wiley.com/doi/pdf/10.1002/2017JC013605.

17. Igneczi, A. & Bamber, J. L. A high-resolution pan-Arctic meltwater discharge dataset from 1950 to 2021. *Earth Syst. Sci. Data* **17**, 3203–3218, 10.5194/essd-17-3203-2025 (2025).

18. Notz, D. & Community, S. Arctic Sea Ice in CMIP6. *Geophys. Res. Lett.* **47**, e2019GL086749, https://doi.org/10.1029/2019GL086749 (2020). E2019GL086749 10.1029/2019GL086749, https://agupubs.onlinelibrary.wiley.com/doi/pdf/10.1029/2019GL086749.

19. Lozier, M. S. *et al.* A sea change in our view of overturning in the subpolar north atlantic. *Sci.* **363**, 516–521, 10.1126/science.aau6592 (2019). https://science.sciencemag.org/content/363/6426/516.full.pdf.

20. Petit, T., Lozier, M. S., Josey, S. A. & Cunningham, S. A. Atlantic Deep Water Formation Occurs Primarily in the Iceland Basin and Irminger Sea by Local Buoyancy Forcing. *Geophys. Res. Lett.* **47**, e2020GL091028, https://doi.org/10.1029/2020GL091028 (2020). E2020GL091028 2020GL091028.

21. Caesar, L., McCarthy, G., Thornalley, D., Cahill, N. & Rahmstorf, S. Current Atlantic Meridional Overturning Circulation weakest in last millennium. *Nat. Geosci.* **14**, 118–120 (2021).

22. Rahmstorf, S. *et al.* Exceptional twentieth-century slowdown in Atlantic Ocean overturning circulation. *Nat. Clim Chang.* **5**, 475–480, 10.1038/nclimate2554 (2015).

23. Caesar, S. R., L., Robinson, A., Feulner, G. & Saba, V. Observed fingerprint of a weakening Atlantic Ocean overturning circulation. *Nat.* **556**, 191–196 (2018).

24. Moat, B. I. *et al.* Pending recovery in the strength of the meridional overturning circulation at 26 N. *Ocean. Sci.* **16**, 863–874, 10.5194/os-16-863-2020 (2020).

25. Ren, Q., Xie, S., Peng, Q., Li, Y. & Wang, F. Equatorial Atlantic mid-depth warming indicates Atlantic meridional overturning circulation slowdown. *Commun Earth Environ* **6**, 819, 10.1038/s43247-025-02793-1 (2025).

26. Pontes, G. & Menviel, L. Weakening of the Atlantic Meridional Overturning Circulation driven by subarctic freshening since the mid-twentieth century. *Nat. Geosci.* https://doi.org/10.1038/s41561-024-01568-1 (2024).

27. He, C. *et al.* A North Atlantic Warming Hole Without Ocean Circulation. *Geophys. Res. Lett.* **49**, e2022GL100420, https://doi.org/10.1029/2022GL100420 (2022). E2022GL100420 2022GL100420, https://agupubs.onlinelibrary.wiley.com/doi/pdf/10.1029/2022GL100420.

28. Johns, W. *et al.* Towards two decades of Atlantic Ocean mass and heat transports at 26.5°N. *Phil. Trans. R. Soc. A.* **381**, 20220188, https://doi.org/10.1098/rsta.2022.0188 (2023).

29. Volkov, D. *et al.* Florida Current transport observations reveal four decades of steady state. *Nat Commun* **15**, 7780, 10.1038/s41467-024-51879-5 (2024).

30. R, B. *et al.* Increased risk of near term global warming due to a recent AMOC weakening. *Nat Commun* **12**, 6108, 10.1038/s41467-021-26370-0 (2021).

31. Terhaar, J., Vogt, L. & Foukal, N. Atlantic overturning inferred from air-sea heat fluxes indicates no decline since the 1960s. *Nat. Commun.* **16**, 222, 10.1038/s41467-024-55297-5 (2025).

32. Zhou, Y. & McManus, J. Heinrich event ice discharge and the fate of the Atlantic Meridional Overturning Circulation. *Sci.* **384**, 983–986, 10.1126/science.adh8369 (2024).

33. Henry, L. *et al.* North Atlantic ocean circulation and abrupt climate change during the last glaciation. *Sci.* **353**, 470–474, 10.1126/science.aaf5529 (2016).

34. Menviel, L. C. *et al.* Enhanced Mid-depth Southward Transport in the Northeast Atlantic at the Last Glacial Maximum Despite a Weaker AMOC. *Paleoceanogr. Paleoclimatology* **35**, e2019PA003793, 10.1029/2019PA003793 (2020). E2019PA003793 10.1029/2019PA003793, https://agupubs.onlinelibrary.wiley.com/doi/pdf/10.1029/2019PA003793.

35. Matero, I., Gregoire, L., Ivanovic, R., Tindall, J. & Haywood, A. The 8.2 ka cooling event caused by Laurentide ice saddle collapse. *Earth Planet. Sci. Lett.* **473**, 205–214, https://doi.org/10.1016/j.epsl.2017.06.011 (2017).

36. Stouffer, R. *et al.* Investigating the causes of the response of the thermohaline circulation to past and future climate changes. *J. Clim.* **19**, 1365–1387 (2006).

37. Kageyama, M. *et al.* Climatic impacts of fresh water hosing under Last Glacial Maximum conditions: a multi-model study. *Clim. Past* **9**, 935–953 (2013).

38. Jackson, L., Kahana, R. & et al., T. G. Global and European climate impacts of a slowdown of the AMOC in a high resolution GCM. *Clim. Dyn.* **45**, 3299–3316, https://doi.org/10.1007/s00382-015-2540-2 (2015).

39. Glaude, Q. *et al.* A Factor Two Difference in 21st-Century Greenland Ice Sheet Surface Mass Balance Projections From Three Regional Climate Models Under a Strong Warming Scenario (SSP5-8.5). *Geophys. Res. Lett.* **51**, e2024GL111902, https://doi.org/10.1029/2024GL111902 (2024). E2024GL111902 2024GL111902, https://agupubs.onlinelibrary.wiley.com/doi/pdf/10.1029/2024GL111902.

40. Ziehn, T. *et al.* The australian earth system model: Access-esm1.5. *J. South. Hemisphere Earth Syst. Sci.* 10.1071/ES19035 (2020).

41. Kiss, A. E. *et al.* ACCESS-OM2 v1.0: a global ocean–sea ice model at three resolutions. *Geosci. Model. Dev.* **13**, 401–442, 10.5194/gmd-13-401-2020 (2020).

42. Greene, C. A., Gardner, A., Wood, M. & Cuzzone, J. Ubiquitous acceleration in Greenland Ice Sheet calving from 1985 to 2022. *Nat.* **625**, 523–528, 10.1038/s41586-023-06863-2 (2024).

43. Rahlves, C., Goelzer, H., Born, A. & Langebroek, P. M. Historically consistent mass loss projections of the Greenland ice sheet. *The Cryosphere,* **19**, 1205–1220, 10.5194/tc-19-1205-2025 (2025).

44. Ziehn, T. *et al.* Access-esm1.5 model output prepared for cmip6 'scenariomip'. v1. *CSIRO. Serv. Collect.* http://hdl.handle.net/102.100.100/422391?index=1 (2019).

45. Bonan, D. *et al.* Observational constraints imply limited future Atlantic meridional overturning circulation weakening. *Nat. Geosci.* **18**, 479–487 (2025).

46. Asbjørnsen, H., Årthun, M., Skagseth, & Eldevik, T. Mechanisms of ocean heat anomalies in the norwegian sea. *J. Geophys. Res. Ocean.* **124**, 2908–2923, https://doi.org/10.1029/2018JC014649 (2019). https://agupubs.onlinelibrary.wiley.com/doi/pdf/10.1029/2018JC014649.

47. Martin, T. & Biastoch, A. On the ocean's response to enhanced Greenland runoff in model experiments: relevance of mesoscale dynamics and atmospheric coupling. *Ocean. Sci.* **19**, 141–167, 10.5194/os-19-141-2023 (2023).

48. Weijer, W., Cheng, W., Garuba, O. A., Hu, A. & Nadiga, B. T. CMIP6 Models Predict Significant 21st Century Decline of the Atlantic Meridional Overturning Circulation. *Geophys. Res. Lett.* **47**, e2019GL086075, 10.1029/2019GL086075 (2020). E2019GL086075 10.1029/2019GL086075, https://agupubs.onlinelibrary.wiley.com/doi/pdf/10.1029/2019GL086075.

49. Swingedouw, D. *et al.* On the risk of abrupt changes in the North Atlantic subpolar gyre in CMIP6 models. *Annals New York Acad. Sci.* **1504**, 187–201, https://doi.org/10.1111/nyas.14659 (2021). https://nyaspubs.onlinelibrary.wiley.com/doi/pdf/10.1111/nyas.14659.

50. He, C. *et al.* North Atlantic subsurface temperature response controlled by effective freshwater input in "Heinrich" events. *Earth Planet. Sci. Lett.* **539**, 116247, 10.1016/j.epsl.2020.116247 (2020).

51. de Boyer Montégut, C. Mixed layer depth climatology computed with a density threshold criterion of 0.03 kg/m3 from 10 m depth value, SEANOE data set, 10.17882/91774 (2023). Accessed: 2025-02-26.

52. Årthun, M., Asbjørnsen, H., Chafik, L., Johnson, H. & Våge, K. Future strengthening of the Nordic Seas overturning circulation. *Nat Commun.* **14**, 2065, 10.1038/s41467-023-37846-6 (2023).

53. Heuzé, C. North atlantic deep water formation and amoc in cmip5 models. *Ocean. Sci.* **13**, 609–622, 10.5194/os-13-609-2017 (2017).

54. Treguier, A. M. *et al.* The mixed-layer depth in the Ocean Model Intercomparison Project (OMIP): impact of resolving mesoscale eddies. *Geosci. Model. Dev.* **16**, 3849–3872, 10.5194/gmd-16-3849-2023 (2023).

55. Barker, S. *et al.* Icebergs not the trigger for North Atlantic cold events. *Nat.* **520**, 333–336 (2015).

56. Goelzer, H. *et al.* The future sea-level contribution of the Greenland ice sheet: a multi-model ensemble study of ISMIP6. *The Cryosphere* **14**, 3071–3096, 10.5194/tc-14-3071-2020 (2020).

57. Curry, W. & Oppo, D. Glacial water mass geometry and the distribution of δ^{13}C of ΣCO_2 in the western Atlantic Ocean. *Paleoceanogr.* **20**, doi:10.1029/2004PA001021 (2005).

58. Paolo, F. S., Fricker, H. A. & Padman, L. Volume loss from antarctic ice shelves is accelerating. *Sci.* **348**, 327–331, 10.1126/science.aaa0940 (2015). http://science.sciencemag.org/content/348/6232/327.full.pdf.

59. Kochtitzky, W. & Copland, L. Retreat of Northern Hemisphere Marine-Terminating Glaciers, 2000–2020. *Geophys. Res. Lett.* **49**, e2021GL096501, https://doi.org/10.1029/2021GL096501 (2022). E2021GL096501 2021GL096501, https://agupubs.onlinelibrary.wiley.com/doi/pdf/10.1029/2021GL096501.

60. Foss, *et al.* Ocean warming drives immediate mass loss from calving glaciers in the high Arctic, journal = Nature Communications, pages = 10460, year = 2024, volume = 15, doi=https://doi.org/10.1038/s41467-024-54825-7. .

61. The HadGEM2 Development Team, N., Bellouin *et al.* The hadgem2 family of met office unified model climate configurations. *Geosci. Model. Dev.* **4**, 723–757 (2011).

62. Kowalczyk, E. *et al.* The land surface model component of access: description and impact on the simulated surface climatology. *Aust. Meteorol. Oceanogr. J.* **63**, 65–82 (2013).

63. Griffies, S. Elements of the modular ocean model (mom): 2012 release (gfdl ocean group technical report no. 7). Tech. Rep., NOAA/Geophysical Fluid Dynamics Laboratory, Princeton, USA (2012).

64. Hunke, E. C., Lipscomb, W. H., Turner, A. K., Jeffery, N. & Elliott, S. Cice: the los alamos sea ice model documentation and software user's manual version 4.1 la-cc-06-012. *T-3 Fluid Dyn. Group, Los Alamos Natl. Lab.* **675**, 500 (2010).

65. Tsujino, H. *et al.* JRA-55 based surface dataset for driving ocean–sea-ice models (JRA55-do). *Ocean. Model.* **130**, 79–139, 10.1016/j.ocemod.2018.07.002 (2018).

66. Mackallah, C. *et al.* ACCESS datasets for CMIP6: methodology and idealised experiments. *J. South. Hemisphere Earth Syst. Sci.* **72**, 93–116, 10.1071/ES21031 (2022).

67. Ziehn, T. *et al.* Csiro access-esm1.5 model output prepared for cmip6 cmip esm-picontrol. version 20210316. *Earth Syst. Grid Fed.* https://doi.org/10.22033/ESGF/CMIP6.4248 (2019).

68. Eyring, V. *et al.* Overview of the Coupled Model Intercomparison Project Phase 6 (CMIP6) experimental design and organization. *Geosci. Model. Dev.* **9**, 1937–1958, 10.5194/gmd-9-1937-2016 (2016).

69. Oliveira Matos, F. D. A. *et al.* Diagnosing the atlantic meridional overturning circulation in density space is critical in warmer climates. *EGUsphere* **2025**, 1–26, 10.5194/egusphere-2025-2326 (2025).

70. Locarnini, R. *et al. World Ocean Atlas 2013*, vol. 1, chap. Temperature, 40 (Ed. NOAA Atlas NESDIS 73, U.S. Government Printing Office, Washington, D.C., 2013).

Acknowledgments Laurie Menviel and Gabriel Pontes acknowledge funding from the Australian Research Council (ARC) grant SR200100008. Himadri Saini and Laurie Menviel acknowledge funding from the ARC grant DP220102134. This research was supported by the Australian Government's National Collaborative Research Infrastructure Strategy (NCRIS), with access to computational resources provided by the National Computational Infrastructure (NCI) through the National Computational Merit Allocation Scheme, and through UNSW (https://researchdata.edu.au/unsw-resource-allocation-scheme-nci/1915200). The authors thank CSIRO for developing the ACCESS-ESM1.5 model configuration and making it freely available to researchers, and thank COSIMA for developing the ACCESS-OM2-025 and making it available. This research used the ACCESS-ESM1.5 and ACCESS-OM2-025 model infrastructures provided by ACCESS-NRI, which is enabled by the Australian Government's NCRIS. The authors would like to thank Peter Dobrohotoff for retrieving the CMIP6 data. The author(s) wish to acknowledge use of the Ferret program for analysis and graphics in this paper. Ferret is a product of NOAA's Pacific Marine Environmental Laboratory. (Information is available at http://ferret.pmel.noaa.gov/Ferret/)

Author contributions statement LM conceived the study, GP performed the experiments, LM analysed the results with help from ML, GP and HS. LM made the figures with the help of GP. LM wrote the manuscript with contributions from GP, HS and ML.

Competing interests statement The authors declare no competing interests.

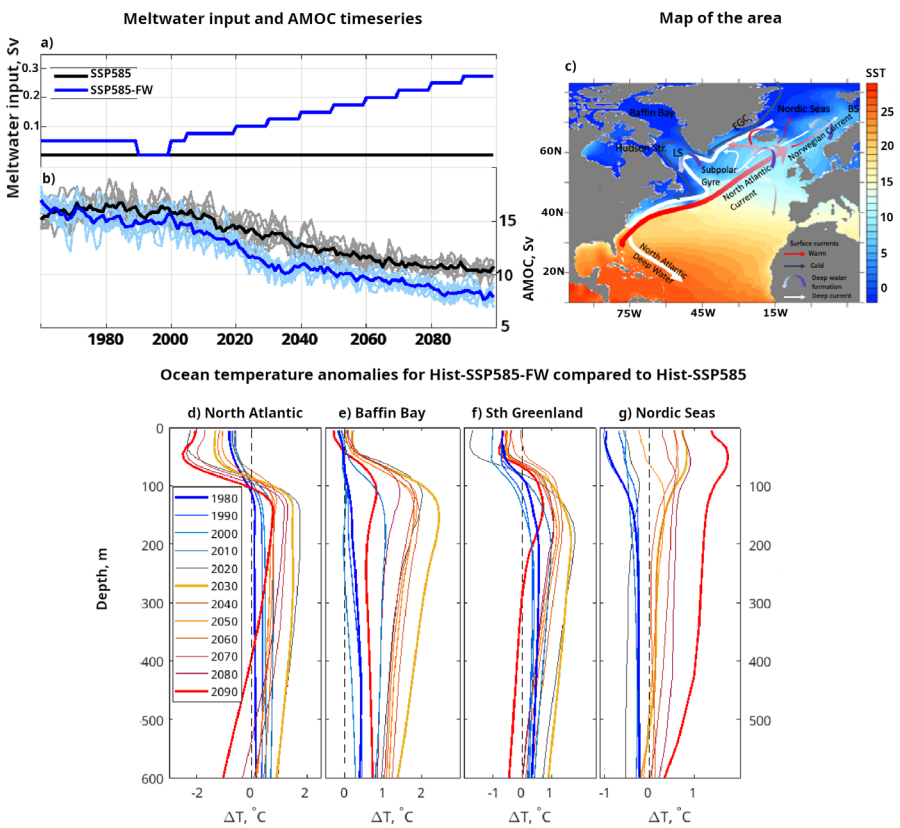

Figure 1. Annual mean timeseries of a) meltwater input (Sv) in the subpolar North Atlantic and b) maximum AMOC transport (Sv) at 26.5°N for potential densities referenced to 2000 dbar of 1035 to 1037 kg/m^3 for the Hist-SSP585-FW (blue) and CMIP6 Hist-SSP585 (black) experiments. The Individual members are in thin pale lines, and the ensemble in thick bright lines. c) Map of the area of interest with main Seas discussed in the text (shading is annual mean SST (70)). LS stands for Labrador Sea, BS for Barents Sea, EGC for East Greenland Current. Ocean temperature anomalies (°C) between the ensemble of Hist-SSP585-FW compared to the ensemble of CMIP6 Hist-SSP585 as a function of depth (m) averaged over d) the subpolar gyre (40°W-20°W, 48°N-62°N); e) Baffin Bay (68°W-50°W, 66°N-76°N); f) the south of Greenland (56°W-38°W, 58°N-68°N) and g) the Nordic Seas (15°W-10°E, 68°N-76°N) averaged over every decades from the 1980s (blue) to 2030s (yellow) and to the 2090s (red). Years 1980-1989, 2030-2039 and 2090-2099 are in bold lines. *MATLAB R2020b was used to generate all subpanels except panel c, which was generated with the Ferret program.*

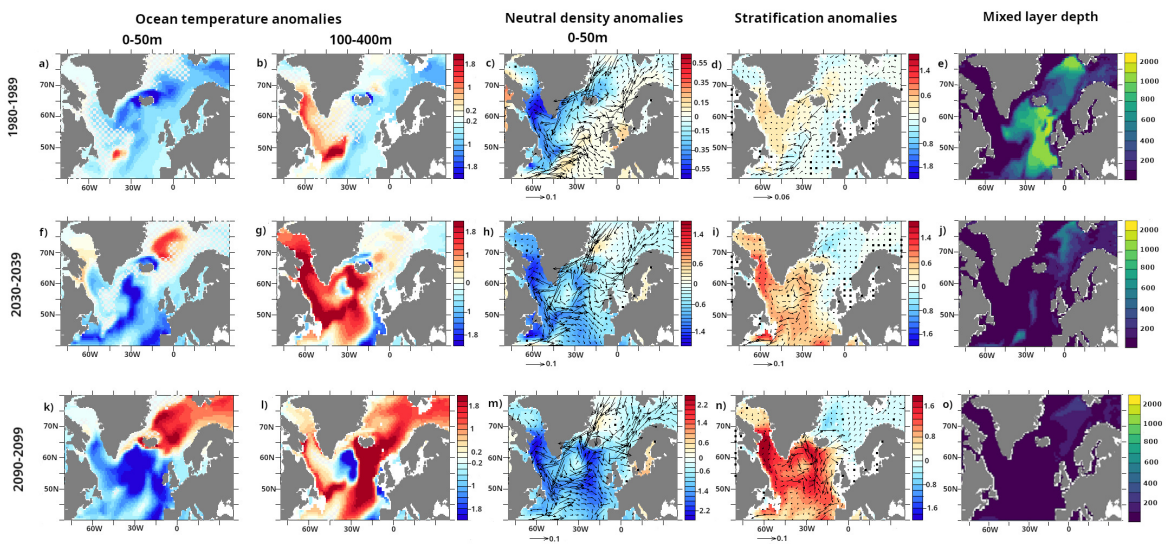

Figure 2. Annual mean ocean temperature anomalies (°C) for (a,f,k) the top 50m and (b,g,l) averaged between 100 and 400m depth; (c,h,m) neutral density anomalies (kg/m^3) for the top 50m with full currents overlaid; (d,i,n) stratification anomalies (kg/m^3) taken as the difference between the neutral density averaged over 100-400m and the surface, with top 50m mean current anomalies overlaid, and (e,j,o) March mixed layer depth (m) for the ensemble mean of Hist-SSP585-FW simulations compared to the ensemble mean of Hist-SSP585 simulations averaged over (top) years 1980-1989, (middle) years 2030-2039 and (bottom) years 2090-2099. The white stippling on the ocean temperature anomalies indicates that at least 2 out of the 8 members disagree on the sign of change. The arrows at the bottom of panels c,d,h,i,m,n represent the current vector key in m/s.

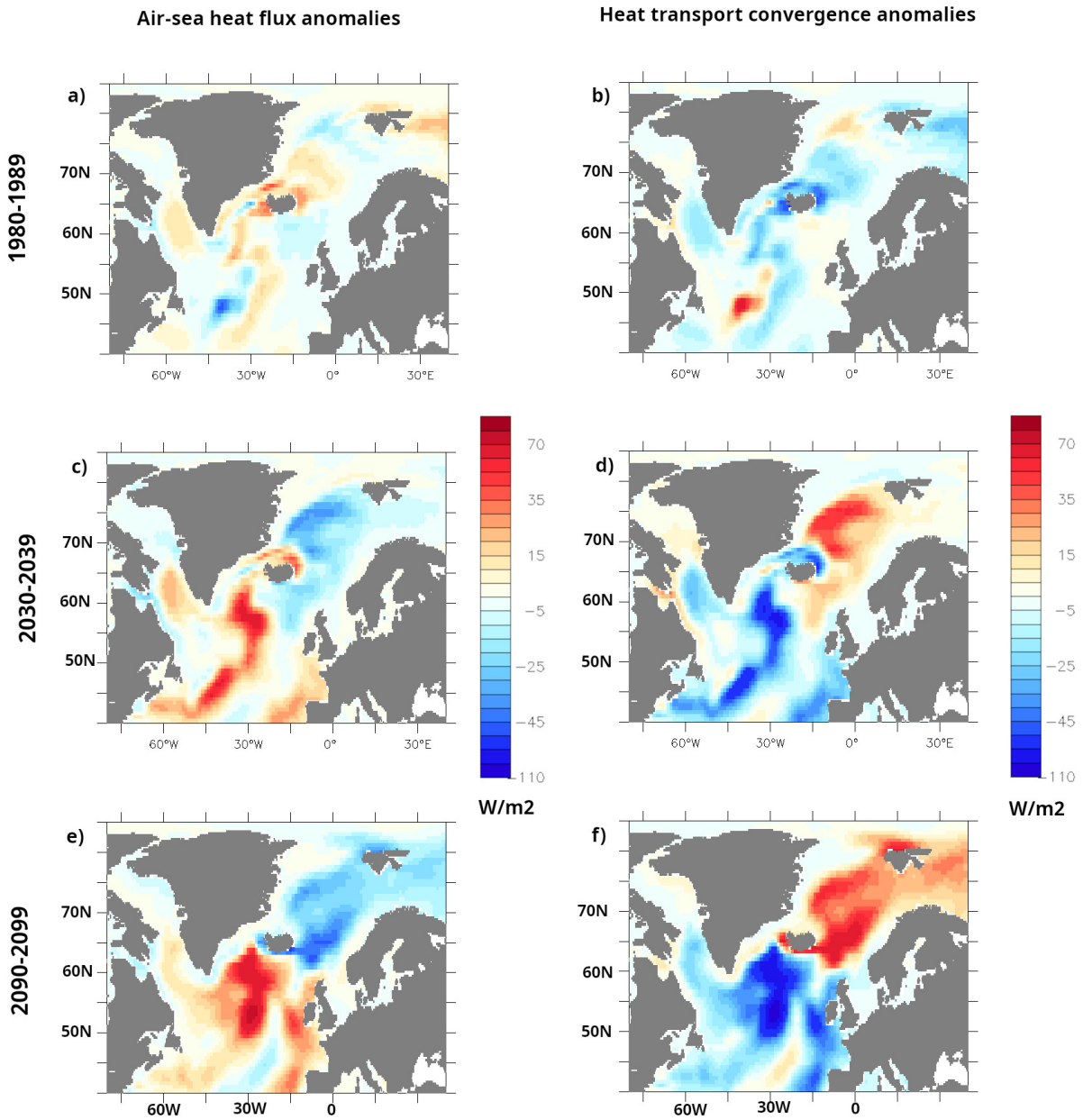

Figure 3. (left) Ocean to atmosphere heat flux anomalies (W/m^2, negative anomalies indicate more heat lost from the ocean or less heat uptake by the ocean) and (right) changes in oceanic heat transport convergence (W/m^2) in the top 50m for the ensemble of Hist-SSP585-FW compared to Hist-SSP585 averaged over years (a,b) 1980-1989, (c,d) 2030-2039, and (e,f) 2090-2099.

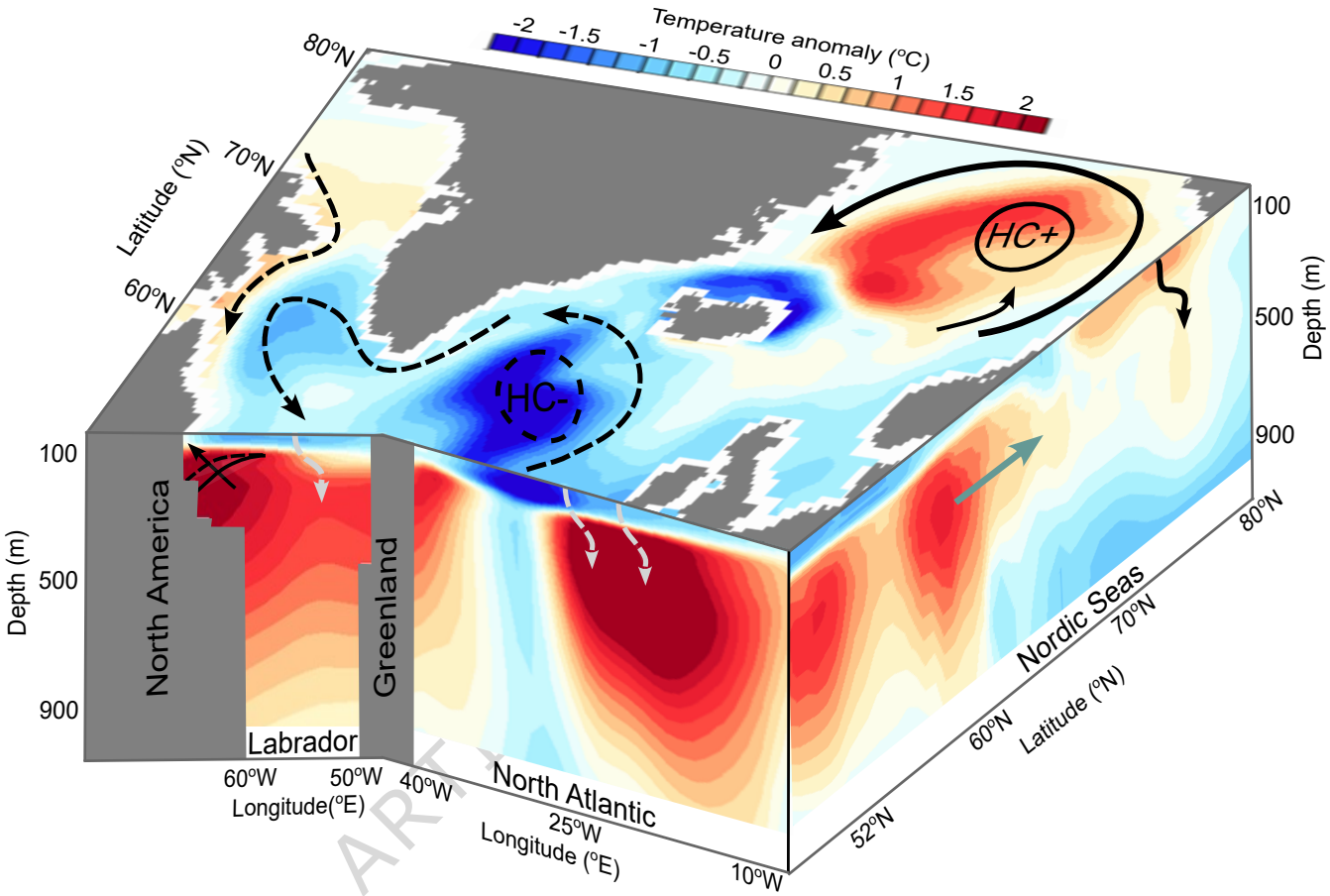

Figure 4. Summary of processes leading to surface (top 50m) and subsurface (0-1000m depth) temperature changes in (lower left side panel) the Labrador Sea (section at 60°N), (centre side panel) the North Atlantic (section at 60°N) and (right side panel) the North Atlantic and Nordic Seas (averaged over 30°W–10°E). Weaker meridional oceanic heat transport towards the North Atlantic (reduced heat convergence, HC-), coupled with a weaker subpolar gyre (dashed black cyclonic circulation) and enhanced stratification (dashed downward arrows) leads to a surface cooling in the North Atlantic, but weaker Baffin Island and Labrador currents (dashed black southward arrow) lead to surface warming in the Hudson Strait and Labrador shelf. Enhanced stratification and reduced convection (grey dashed downward arrows) lead to a subsurface warming in the North Atlantic, Baffin Bay and the Labrador Sea - with a flattening of the isopycnals (solid and dashed lines with side arrows) allowing for incursion of warmer water onto the shelf in the Labrador Sea. A stronger cyclonic circulation in the Nordic Seas (black cyclonic loop), with stronger Norwegian Atlantic Front Current and Norwegian Atlantic Slope Current (and increased heat convergence, HC+), increases the density of surface waters in the central Nordic Seas, reducing stratification and leading to a surface and subsurface warming. A transient stronger Atlantic inflow could further warm the Nordic Seas (green arrow).

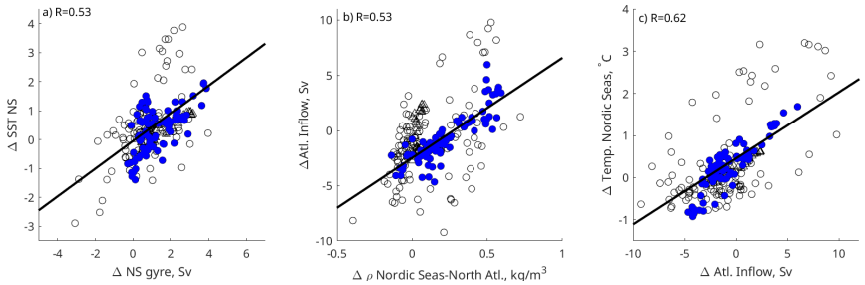

Figure 5. Changes in Nordic Seas SST and subsurface temperature as a function of the Nordic Sea circulation and Atlantic inflow (Sv) in experiments performed with the ACCESS-ESM1.5 (circles, ensemble of SSP585-FW compared to the ensemble of SSP585 in blue, FW04-ESM in black) and the ACCESS-OM2-025 (black triangles, FW0075-OM). Each point represents annual mean anomalies for each experiment compared to their control and over the course of the experiment. a) Nordic Seas SST anomaly (15°W-10°E, 68°N-76°N, °C) as a function of the maximum cyclonic barotropic streamfunction in the Nordic Seas (Sv). b) Northward Atlantic inflow (Sv) as a function of the density difference between the Nordic Seas (15°W-5°E, 66°N-75°N, 0-400m depth) and the North Atlantic (25°W-5°W, 58°N-64°N, 0-400m depth). c) Nordic Seas ocean temperature anomaly (15°W-15°E, 68°N-76°N, 100-400m depth, °C) as a function of the Atlantic inflow (Sv). The Atlantic inflow is calculated as the meridional transport between 18°W and 0°E and the first 400m depth at 64°N. For the ACCESS-OM2, the Atlantic inflow is narrower and thus taken as the meridional transport between 2°W and 2°E. Overall correlations for all the experiments are displayed on the graph. For the Hist-SSP585-FW compared to Hist-SSP585 ensembles, correlations are 0.6, 0.87 and 0.88 for a-c, respectively. *MATLAB R2020b was used to generate this graph.*

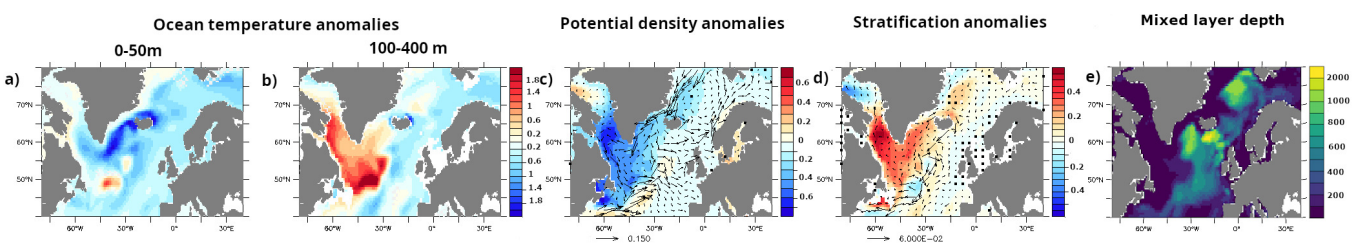

Figure 6. Annual mean ocean temperature anomaly (°C) for (a) the top 50m, and (b) averaged between 100 and 400m depth; (c) neutral density anomaly (kg/m^3) with currents (m/s) overlaid for the top 50m; (d) stratification anomaly (kg/m^3) defined as the difference between the 100-400m neutral density and the surface neutral density for experiment FW005-ESM compared to the control run and averaged over years 20 to 50. (e) March mixed layer depth (m) for experiment FW005-ESM. White stippling in a) and b) indicates that less than 3 out 4 of simulations of the ensemble agree on the sign of change (mostly around Svalbard). The arrows at the bottom of panels c and d present the current vector key in m/s.

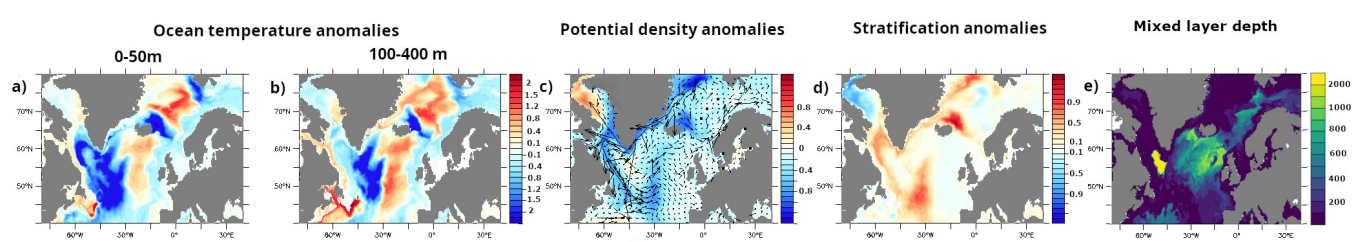

Figure 7. Annual mean ocean temperature anomaly (°C) for (a) the top 50m, and (b) averaged between 100 and 400m depth; (c) neutral density anomaly (kg/m^3) with currents (m/s) overlaid for the top 50m; (d) stratification anomaly (kg/m^3) defined as the difference between the 100-400m potential density and the surface potential density for experiment FW0075-OM compared to the control run and averaged over years 20 to 40. (e) March mixed layer depth (m) for experiment FW0075-OM. The arrow at the bottom of panel c represents the current vector key in m/s.

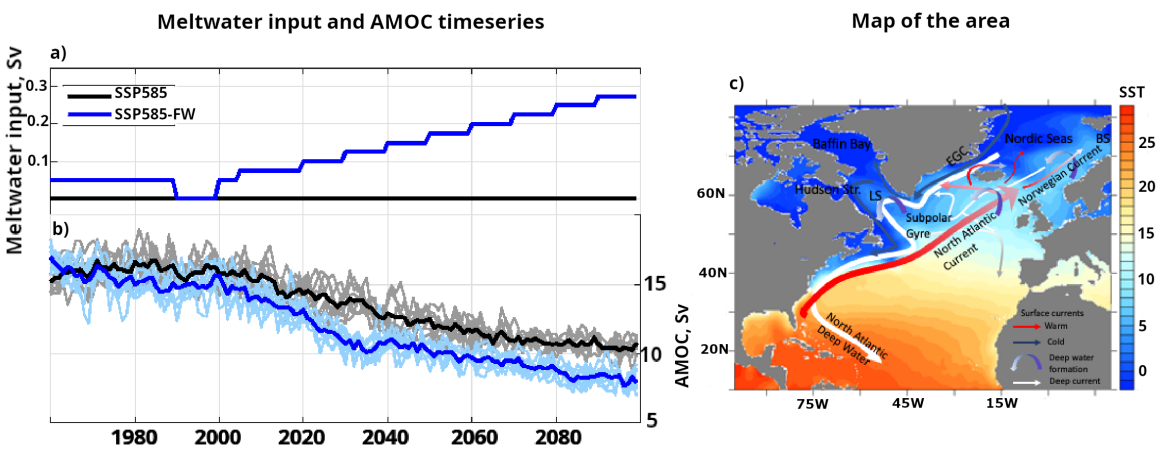
Meltwater input and AMOC timeseries
Map of the area
a)
b)
c)
Meltwater input, Sv
SSP585
SSP585-FW
AMOC, Sv
SST
Baffin Bay
Nordic Seas
Hudson Str.
LS
EGC
BS
Norwegian Current
Subpolar Gyre
North Atlantic Current
North Atlantic Deep Water
Surface currents
Warm
Cold
Deep water formation
Deep current
60N
40N
20N
75W
45W
15W
1980
2000
2020
2040
2060
2080

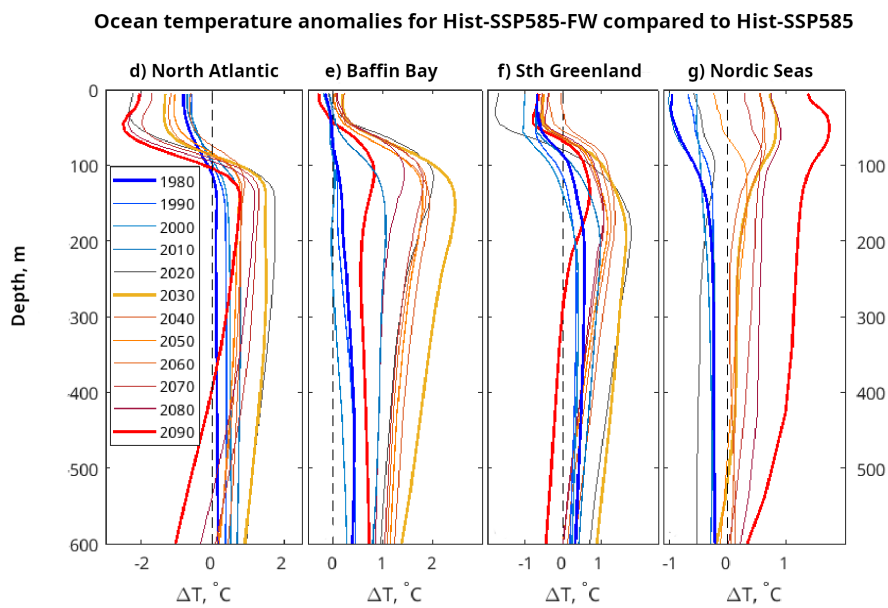
Ocean temperature anomalies for Hist-SSP585-FW compared to Hist-SSP585
d) North Atlantic
e) Baffin Bay
f) Sth Greenland
g) Nordic Seas
Depth, m
ΔT, ˚C
1980
1990
2000
2010
2020
2030
2040
2050
2060
2070
2080
2090

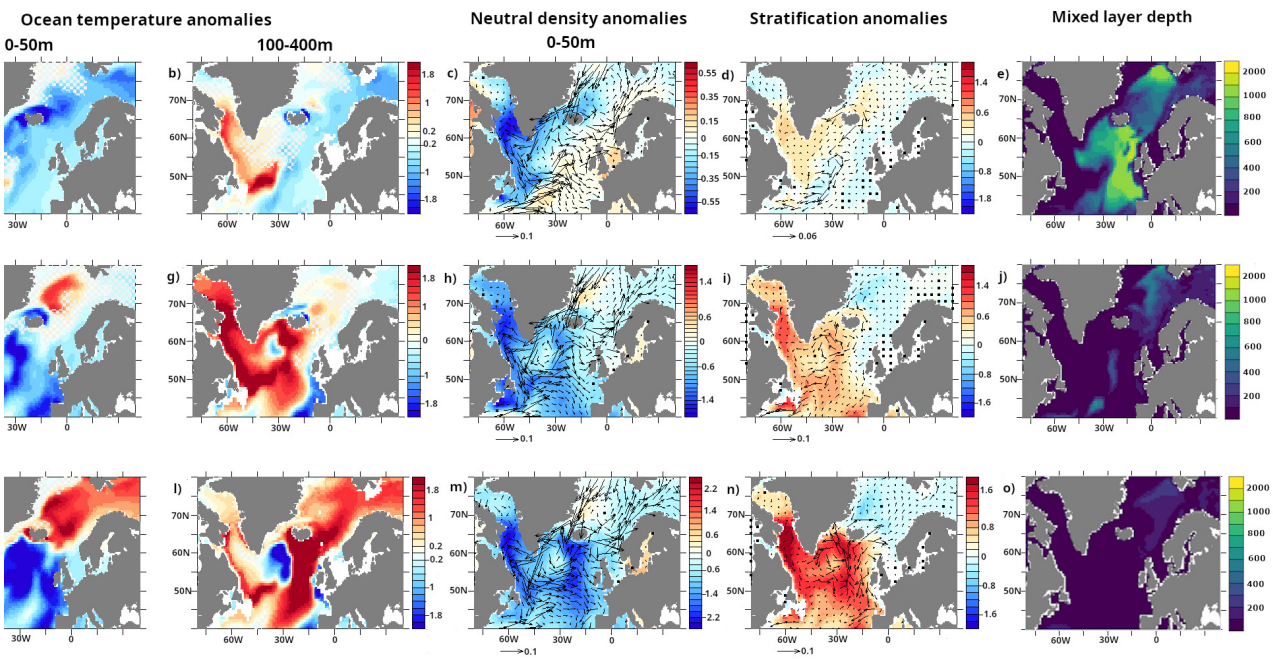
Ocean temperature anomalies
0-50m
100-400m
Neutral density anomalies
0-50m
Stratification anomalies
Mixed layer depth
a)
b)
c)
d)
e)
g)
h)
i)
j)
l)
m)
n)
o)
70N
60N
50N
60W
30W
0
0.1
0.06

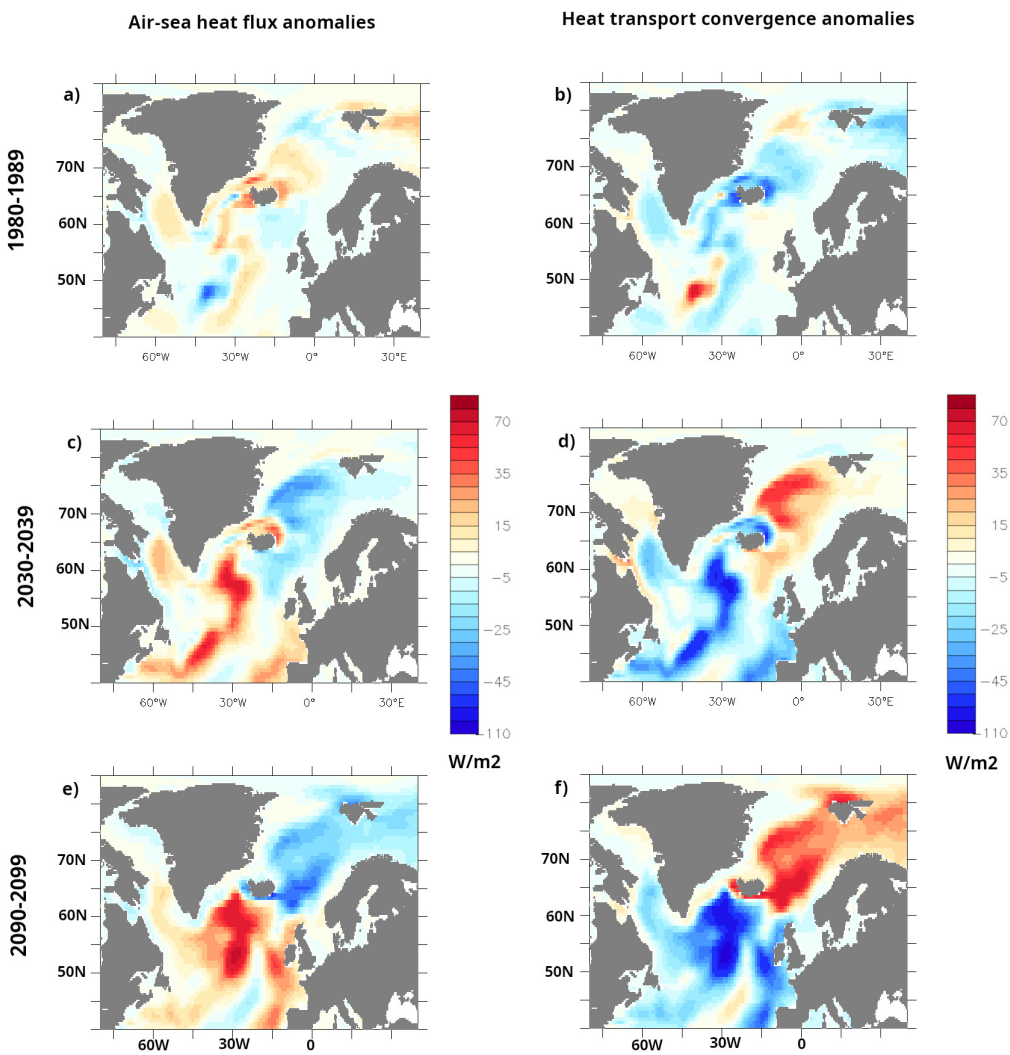
Air-sea heat flux anomalies
Heat transport convergence anomalies
1980-1989
2030-2039
2090-2099
a)
b)
c)
d)
e)
f)
70N
60N
50N
60°W
30°W
0°
30°E
60W
30W
0
70
35
15
−5
−25
−45
−110
W/m2

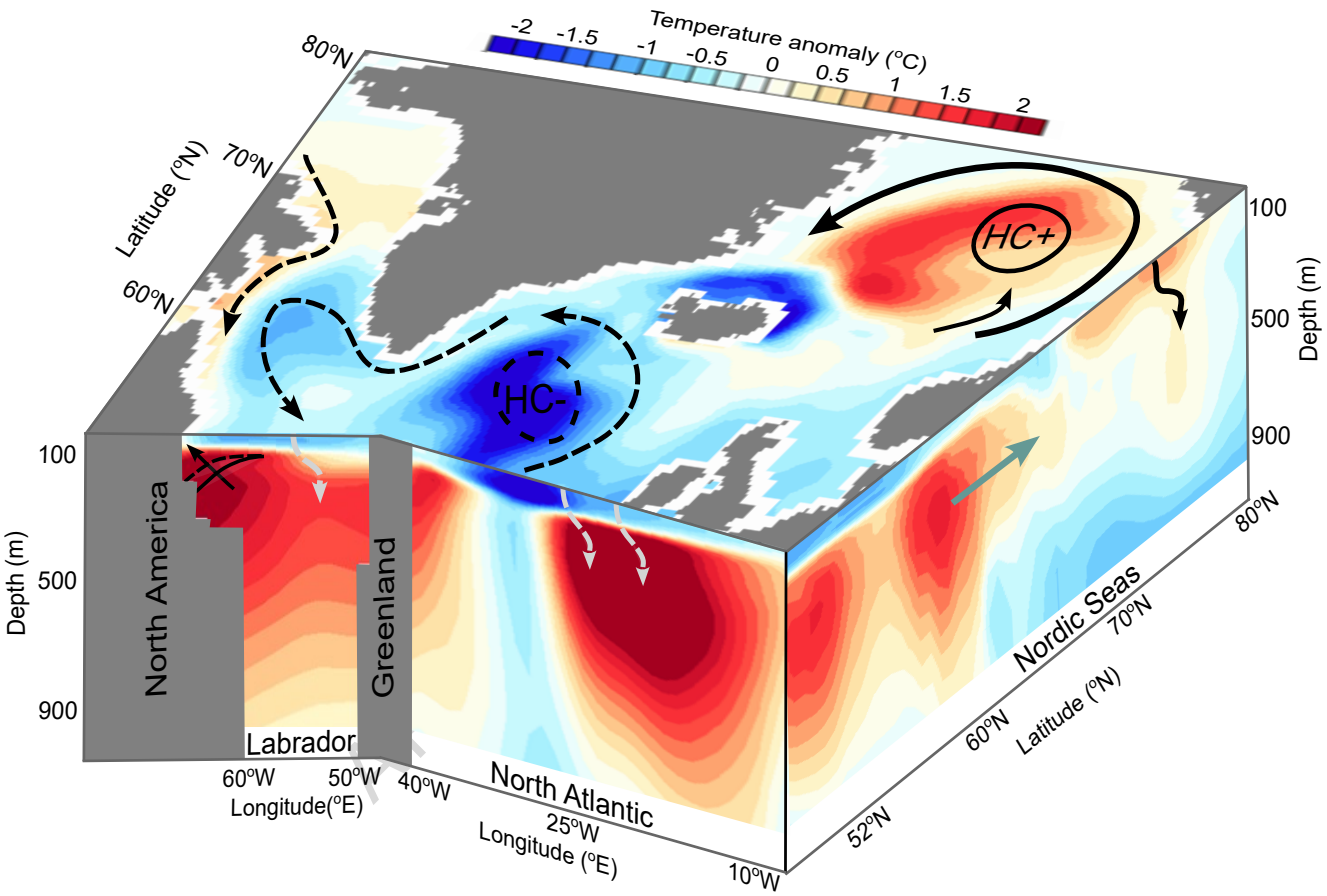
Temperature anomaly (°C)
-2
-1.5
-1
-0.5
0
0.5
1
1.5
2
80°N
70°N
60°N
Latitude (°N)
HC+
HC-
100
500
900
Depth (m)
North America
Greenland
Labrador
60°W
50°W
40°W
Longitude(°E)
North Atlantic
25°W
10°W
Longitude (°E)
Nordic Seas
52°N
60°N
70°N
80°N
Latitude (°N)